Supplementary Information

A Theory

A.1 Scope of model

Because of thermal fluctuations, a polymer chain at room temperature will be bent. WLC and our model both predict that the molecule's observed conformations will be drawn from a certain probability distribution of shapes, obtained by combining bends distributed according to Boltzmann statistics with some energy function $E(\theta)$. Our task is to evaluate $E(\theta)$ from data.

A comprehensive theory of DNA bending on short length scales must also include the twist degrees of freedom (*1*), as well as inhomogeneities from sequence (*2, 3*). Indeed, recent cyclization experiments suggest that the harmonic-elasticity model for the twist response of DNA also overstates the energetic cost of twist when curvature is high (*4*). Thus, it seems likely that the twist energy function must be modified in a manner analogous to the one we have proposed for the bending energy. We leave this generalizations to future work. As for bending anisotropy and sequence dependence, for the random sequences studied here we expect them to be small effects for behavior on length scales greater than the helical pitch of 3.5 nm.

A.2 Scale dependence in equilibrium statistical physics

Here we briefly elaborate on some ideas of scale dependence in equilibrium statistical physics, applied to our problem.

The conformation of a macromolecule like DNA can usefully be described on any of several length scales. That is, when describing the molecule's behavior on a length scale $\ell_{\rm exp}$ larger than the size of individual atoms, we can often simplify our description by imagining the macromolecule to be composed of effective elements of some size ℓ shorter than $\ell_{\rm exp}$. Simple effective interactions among the ele-

ments then suffice to reproduce the collective behavior of the molecule, despite its underlying structural complexity (*5*).

We choose to examine the conformation of DNA only on scales longer than the apparent width $\ell_{\rm exp} \approx 5\,$nm shown in Fig. 1**b**. The mesoscopic theory describes only a reduced set of "coarse-grained degrees of freedom," describing the overall behavior observed by experiments on scales longer than $\ell_{\rm exp}$. In our case, the mesoscopic degree of freedom is an angle describing the orientation of each successive link in a two-dimensional chain.

We expect to be able to describe our system's physical behavior on scales $\geq \ell_{\rm exp}$ by an effective mesoscopic model, discretized at some scale ℓ that is shorter than $\ell_{\rm exp}$. We chose $\ell = 2.5\,$nm; other choices would also work. The model is characterized by an "effective elastic-energy function" $E(\{\theta_i\};\ell)$. (In the main text we suppressed mention of the scale ℓ, because it was always fixed to $2.5\,$nm.) The effective model could in principle be derived by an averaging process, starting with an underlying microscopic model. In practice, however, one can often impose symmetries that restrict the possible forms of the function E to the point where it can be directly obtained from experiment, as we do here. For example, the bending energy functions we consider are symmetric under $\theta \to -\theta$ (except in Sect. D.2 below).

The assumption of local interactions requires comment. Both WLC and our model assume that each joint bends independently of the others; the effects of long-range electrostatic interactions and conformational cooperativity, if any, are assumed to be irrelevant for behavior on length scales greater than $\ell_{\rm exp}$, which in our experiments was as small as $5\,$nm. In typical solvent conditions, where the Debye screening length is less than $5\,$nm, this assumption is reasonable. Then the distribution function $g(\hat{t}_{i+1}|\hat{t}_i)$ completely determines all polymer distribution functions and observables. Even if there are nonlocal interactions at the microscopic level (for example reflecting conformational cooperativity between the physical subunits (*6*)), nevertheless there may still be a length scale beyond which these are unimportant. Thus we consider locality as a hypothesis to test, by dropping any possible nonlocal terms in E, that is, by taking $E = \sum_i E(\theta_i;\ell)$ where θ_i is the bending angle at position i. Hence the

bend angle distributions all take the form given in the main text:

$$g(\hat{t}_{i+1}|\hat{t}_i) = q^{-1}\exp[-E(\theta_i)/k_{\mathrm{B}}T], \tag{2}$$

In WLC, the relation between discretizations on different scales is extremely simple: The energy functions $E(\theta;\ell_1) = (\xi/2\ell_1)\theta^2$, discretized on ℓ_1, and $E(\theta;\ell_2) = (\xi/2\ell_2)\theta^2$, discretized on ℓ_2, give equivalent results on length scales longer than either ℓ_1 or ℓ_2. In other local elasticity models, however, the relation is not so simple. In fact, our work illustrates a general result from renormalization-group theory: Models that are different when viewed on one scale may be nearly indistinguishable when viewed on longer scales.

Because the discretization scale ℓ is to some extent arbitrary, not all apparent differences between effective elastic energy functions with different ℓ are physically significant. In particular, our energy function $E_{\mathrm{LSEC}}(\theta; 2.5\mathrm{nm}) = \alpha|\theta|k_{\mathrm{B}}T$ is nonanalytic (it has a sharp point at $\theta = 0$), but this feature is not physically significant: We could have derived the same behavior from a different-looking model, discretized with $\ell' = 5\,\mathrm{nm}$. That theory's effective elastic energy function can be obtained by taking the convolution of $\mathrm{e}^{-E_{\mathrm{LSEC}}(\theta)/k_{\mathrm{B}}T}$ with itself; it does not have a sharp point at $\theta = 0$, although it does retain the characteristic linear behavior at larger θ. (Indeed this function is essentially the solid red curve in Fig. 3**a**.) What is physically significant are predictions on experimentally measurable scales that differ from the predictions of WLC.

Even if the molecule is externally confined, analysis of its conformations may still give useful information about the free bending-energy function. For example, adsorption of the molecule to a planar surface may leave it free to bend within the plane. In that case we may expect that the appropriate distribution will be given by an effective bending energy function restricted to tangent vectors in the plane but with the same general form as the one appropriate for molecules in free solution.

A.3 Model-independent tests

Given any two-dimensional, local-elasticity model characterized by $g(\hat{t}_{i+1}|\hat{t}_i)$, we define the persistence length ξ by $\langle\cos\theta_{s,s+\ell}\rangle = \mathrm{e}^{-\ell/(2\xi)}$. Then for separations greater than the segment length ℓ we have

$\langle \cos\theta_{s,s+L} \rangle = \mathrm{e}^{-L/(2\xi)}$ and (*7*)

$$\langle (R_{s,s+L})^2 \rangle = 4\xi \left(L + 2\xi(\mathrm{e}^{-L/(2\xi)} - 1) \right).$$

This formula was also used by Rivetti et al. (*8*), who considered only the particular case of WLC.

A.4 Tests that distinguish different models

In the class of models we study, the angle-angle correlation of neighboring chain segments determines all statistical properties of the polymer. We chose to examine both the angle-angle correlation $G(\theta; L)$ of points at arbitrary separation, and the distribution $K(R; L)$ of real-space distance R between pairs of points at fixed arc-length separation L. The distribution G has a more direct physical meaning than K. However, K is less sensitive than G to small errors in point placement potentially made by the image-analysis software, so it serves as a useful additional check on our results. Fig. 3 shows that the predictions of our model for both distributions are successful with no further fitting, once the single parameter α is chosen to reproduce the large-L data. WLC cannot be made to fit all length scales simultaneously.

A.5 Relation to other work

The detailed, atomic-length-scale response of a macromolecule to external stresses is complex; for example, DNA in protein complexes has long been known to involve kinked conformations (*9, 10*).

The idea that DNA may undergo local elastic breakdown under external stress is not new or surprising. But the implications of such breakdown for *spontaneous* fluctuations, and the use of those fluctuations to measure the mesoscale effective bending energy function, have received little attention, despite some hints in earlier, less detailed measurements. For example, small but significant deviation from WLC behavior at distances less than ξ can be seen in data on the moments of the tangent angle distribution (*8*). The behavior we found in the angle-angle correlation was also partly visible in earlier, lower-resolution AFM studies (*11*). More recently, two groups wrote DNA models incorporating elastic breakdown at high curvature (*12, 13*) (see also (*14, 15*)). Although these "spontaneous kinking"

models differ in detail, they describe essentially similar physics. Both suppose that DNA has a normal conformation with harmonic bend elasticity, but can pop spontaneously into an alternate, highly flexible conformation (for example via local DNA melting (*12*)). The energy needed for this conformational change is a new model parameter, which the authors set by demanding agreement with recent measurements on the cyclization of 96-basepair constructs (*16, 4*). Recently, however, these experimental results have been called into question (*17*), and in any case this approach does not empirically determine the form of the bending energy function, as we have done here.

Du et al. did attempt an indirect determination of the bending energy function (*17*). They tabulated the incidence of various static bends in DNA-protein complexes listed in the Protein Database, then used these frequencies as a rough guide to the bending energy of the DNA itself. Although they noted that the bend frequencies in complexed DNA are not expected to agree quantitatively with those of free DNA, nevertheless their bending energy function and ours have similar qualitative features (see Sect. D.5).

Shroff et al. experimentally measured the fluctuation behavior of short loops containing a force reporter, and found that the bending stress needed to create such a loop is much smaller than predicted by WLC, but in rough accord with our prediction (*18, 7*). Finally, a recent all-atom molecular dynamics simulation of open DNA has also shown an unexpectedly high incidence of spontaneous, large-angle bends (J.Z. Ruscio and A. Onufriev, unpublished).

Our experiments do not show the detailed molecular structure of the sharp bends. Yan and Marko proposed that they could be melted segments (*12*). But DNA melting is not seen in the sharp bends that occur in molecular dynamics simulations of DNA minicircles (F. Lankas, R. Lavery and J.H. Maddocks, unpublished). Similarly, recent simulations of open DNA show a high incidence of spontaneous, large-angle bends without any breaking of Watson–Crick pairs (J.Z. Ruscio and A. Onufriev, unpublished). Indeed, even the kinks observed experimentally in protein–DNA complex structures, for example the one in Ref. (*10*), do not appear to be melted. Finally, when a tight loop forms between two operator sites, several regularly spaced, sharply defined sites of DNAse hypersensitivity appear (*19*). If the DNA underwent a complete elastic breakdown, we would expect only a single, poorly defined site of

sensitivity to digestion.

The main text suggested the alternative hypothesis of a thermodynamic coexistence of alternate conformers, some of them bent. Long ago, Song and Schurr made the closely related proposal that measured differences between the static and dynamic stiffnesses of DNA could be explained by a complex energy landscape associated with small deflections (*20*).

B Materials and Methods

B.1 Sample preparation, AFM imaging, and control experiments

The construct used in our experiments is pGEM-3Z (Promega). The sequence is shown in Table S1. This natural DNA does not contain phased A-tracts, which lead to large intrinsic bends (*21*). A variety of experimental and theoretical works have shown that, for random DNA, sequence inhomogeneity can simply be regarded as effectively giving a contribution to the persistence length (reviewed in (*22*)), and indeed this contribution itself appears to be small (*23*). Visual inspection of the images showed that the surface and the DNA were free of any salt deposits or protein impurities, which could potentially introduce large bends in the adhered DNA molecules.

Standard checks showed that DNA molecules were equilibrated, as described in the main text. Different salt concentrations yielded the same $G(\theta; L)$ distribution (Fig. S1). Use of [Mg^{2+}] lower than 6 mM yielded loosely bound DNA molecules. The lack of a strong ion-strength dependence argues against a model of total elastic breakdown: The resulting sharp bends would be strongly electrostatically suppressed at low ionic strength (J.Z. Ruscio and A. Onufriev, unpublished). Ref. (*24*) gives another study of the influence of ionic conditions on adsorbed DNA.

It could be argued that the presence of nicks may induce large bends in the contour of adsorbed DNA molecules. To address this issue, we grew the commercial plasmid pGEM-3Z in bacteria, minimizing already the presence of nicks. The plasmid was linearized with BamH I and Sca I leading to sticky and blunt ends respectively. Then we incubated both samples with *E. coli* DNA ligase (New England Biolabs, Ipswich, MA, USA). This ligase is extremely inefficient in ligating blunt ends. Therefore no

band shift was detected in the blunt-ends sample, whereas a clear shift was detected in the control sticky-ends one (data not shown). This experiment confirmed that our ligation reaction worked properly; hence we expect a nick-free sample. Ligase-treated samples showed the same results as described in the main text (Fig. S2 and Table S2).

We also compared the highest available mica quality (grade V1) to the results on V4 mica reported in the main text; the results were similar (Fig. S3 and Table S2).

Ultra-sharp tips occasionally caused physical breakage of DNA molecules. This was evidenced in further scans. These artifacts were detected at salt concentrations lower than used to generate the data in the main text. Nevertheless, to test if spurious breaks pose a significant issue for us, we reasoned that this phenomenon if present would induce a correlation between large-angle bends and the absolute orientation of the DNA chain: There would be more large-angle bends when the chain is oriented perpendicular to the raster scan lines. Fig. S4 shows that this concern was not realized at the salt concentration used to obtain the data in the main text.

1	GGGCGAATTC GAGCTCGGTA CCCGGGGATC CTCTAGAGTC GACCTGCAGG	1401	CCGCGAGACC CACGCTCACC GGCTCCAGAT TTATCAGCAA TAAACCAGCC
51	CATGCAAGCT TGAGTATTCT ATAGTGTCAC CTAAATAGCT TGGCGTAATC	1451	AGCCGGAAGG GCCGAGCGCA GAAGTGGTCC TGCAACTTTA TCCGCCTCCA
101	ATGGTCATAG CTGTTTCCTG TGTGAAATTG TTATCCGCTC ACAATTCCAC	1501	TCCAGTCTAT TAATTGTTGC CGGGAAGCTA GAGTAAGTAG TTCGCCAGTT
151	ACAACATACG AGCCGGAAGC ATAAAGTGTA AAGCCTGGGG TGCCTAATGA	1551	AATAGTTTGC GCAACGTTGT TGCCATTGCT ACAGGCATCG TGGTGTCACG
201	GTGAGCTAAC TCACATTAAT TGCGTTGCGC TCACTGCCCG CTTTCCAGTC	1601	CTCGTCGTTT GGTATGGCTT CATTCAGCTC CGGTTCCCAA CGATCAAGGC
251	GGGAAACCTG TCGTGCCAGC TGCATTAATG AATCGGCCAA CGCGCGGGGA	1651	GAGTTACATG ATCCCCCATG TTGTGCAAAA AAGCGGTTAG CTCCTTCGGT
301	GAGGCGGTTT GCGTATTGGG CGCTCTTCCG CTTCCTCGCT CACTGACTCG	1701	CCTCCGATCG TTGTCAGAAG TAAGTTGGCC GCAGTGTTAT CACTCATGGT
351	CTGCGCTCGG TCGTTCGGCT GCGGCGAGCG GTATCAGCTC ACTCAAAGGC	1751	TATGGCAGCA CTGCATAATT CTCTTACTGT CATGCCATCC GTAAGATGCT
401	GGTAATACGG TTATCCACAG AATCAGGGGA TAACGCAGGA AAGAACATGT	1801	TTTCTGTGAC TGGTGAGTAC TCAACCAAGT CATTCTGAGA ATAGTGTATG
451	GAGCAAAAGG CCAGCAAAAG GCCAGGAACC GTAAAAAGGC CGCGTTGCTG	1851	CGGCGACCGA GTTGCTCTTG CCCGGCGTCA ATACGGGATA ATACCGCGCC
501	GCGTTTTTCC ATAGGCTCCG CCCCCCTGAC GAGCATCACA AAAATCGACG	1901	ACATAGCAGA ACTTTAAAAG TGCTCATCAT TGGAAAACGT TCTTCGGGGC
551	CTCAAGTCAG AGGTGGCGAA ACCCGACAGG ACTATAAAGA TACCAGGCGT	1951	GAAAACTCTC AAGGATCTTA CCGCTGTTGA GATCCAGTTC GATGTAACCC
601	TTCCCCCTGG AAGCTCCCTC GTGCGCTCTC CTGTTCCGAC CCTGCCGCTT	2001	ACTCGTGCAC CCAACTGATC TTCAGCATCT TTTACTTTCA CCAGCGTTTC
651	ACCGGATACC TGTCCGCCTT TCTCCCTTCG GGAAGCGTGG CGCTTTCTCA	2051	TGGGTGAGCA AAAACAGGAA GGCAAAATGC CGCAAAAAAG GGAATAAGGG
701	TAGCTCACGC TGTAGGTATC TCAGTTCGGT GTAGGTCGTT CGCTCCAAGC	2101	CGACACGGAA ATGTTGAATA CTCATACTCT TCCTTTTTCA ATATTATTGA
751	TGGGCTGTGT GCACGAACCC CCCGTTCAGC CCGACCGCTG CGCCTTATCC	2151	AGCATTTATC AGGGTTATTG TCTCATGAGC GGATACATAT TTGAATGTAT
801	GGTAACTATC GTCTTGAGTC CAACCCGGTA AGACACGACT TATCGCCACT	2201	TTAGAAAAAT AAACAAATAG GGGTTCCGCG CACATTTCCC CGAAAAGTGC
851	GGCAGCAGCC ACTGGTAACA GGATTAGCAG AGCGAGGTAT GTAGGCGGTG	2251	CACCTGACGT CTAAGAAACC ATTATTATCA TGACATTAAC CTATAAAAAT
901	CTACAGAGTT CTTGAAGTGG TGGCCTAACT ACGGCTACAC TAGAAGAACA	2301	AGGCGTATCA CGAGGCCCTT TCGTCTCGCG CGTTTCGGTG ATGACGGTGA
951	GTATTTGGTA TCTGCGCTCT GCTGAAGCCA GTTACCTTCG GAAAAAGAGT	2351	AAACCTCTGA CACATGCAGC TCCCGGAGAC GGTCACAGCT TGTCTGTAAG
1001	TGGTAGCTCT TGATCCGGCA AACAAACCAC CGCTGGTAGC GGTGGTTTTT	2401	CGGATGCCGG GAGCAGACAA GCCCGTCAGG GCGCGTCAGC GGGTGTTGGC
1051	TTGTTTGCAA GCAGCAGATT ACGCGCAGAA AAAAAGGATC TCAAGAAGAT	2451	GGGTGTCGGG GCTGGCTTAA CTATGCGGCA TCAGAGCAGA TTGTACTGAG
1101	CCTTTGATCT TTTCTACGGG GTCTGACGCT CAGTGGAACG AAAACTCACG	2501	AGTGCACCAT ATGCGGTGTG AAATACCGCA CAGATGCGTA AGGAGAAAAT
1151	TTAAGGGATT TTGGTCATGA GATTATCAAA AAGGATCTTC ACCTAGATCC	2551	ACCGCATCAG GCGCCATTCG CCATTCAGGC TGCGCAACTG TTGGGAAGGG
1201	TTTTAAATTA AAAATGAAGT TTTAAATCAA TCTAAAGTAT ATATGAGTAA	2601	CGATCGGTGC GGGCCTCTTC GCTATTACGC CAGCTGGCGA AAGGGGGATG
1251	ACTTGGTCTG ACAGTTACCA ATGCTTAATC AGTGAGGCAC CTATCTCAGC	2651	TGCTGCAAGG CGATTAAGTT GGGTAACGCC AGGGTTTTCC CAGTCACGAC
1301	GATCTGTCTA TTTCGTTCAT CCATAGTTGC CTGACTCCCC GTCGTGTAGA	2701	GTTGTAAAAC GACGGCCAGT GAATTGTAAT ACGACTCACT ATA
1351	TAACTACGAT ACGGGAGGGC TTACCATCTG GCCCCAGTGC TGCAATGATA		

Table S1: DNA sequence used.

	Points separated by $L = 5$ nm					Points sep. by $L = 10$ nm		
	# pairs	# large	**fraction**	# med	**fraction**	# pairs	# large	**fraction**
Exp. data	93 895	82	**0.000 87**	746	**0.0079**	92 725	969	**0.010**
Exp.,Ligase	51 303	42	**0.000 82**	469	**0.0091**	50 699	467	**0.0092**
Exp., V1	30 597	18	**0.000 59**	263	**0.0086**	30 263	326	**0.011**
WLC	3 122 109	91	**0.000 029**	6848	**0.0022**	3 105 187	17 678	**0.0057**
WLC,sim.	200 152	11	**0.000 055**	568	**0.0028**	185 164	1089	**0.0059**
LSEC,Eq. (1)	2 922 111	2756	**0.000 94**	21 809	**0.0075**	2 906 273	28 773	**0.0099**

Table S2: Control experiments and simulations discussed in the text. The table reproduces Table 1 in main text (see its caption), with three additional rows. Row 2 gives the incidence of bends for DNA incubated with ligase. Row 3 gives the incidence of bends when DNA was adsorbed to V1-grade mica. Row 5 gives numerical results when WLC configurations generated by the Monte Carlo code (row 4) were converted to simulated AFM traces and then sent through our image analysis (solid curve in Fig. 2**c**, and Fig. S8).

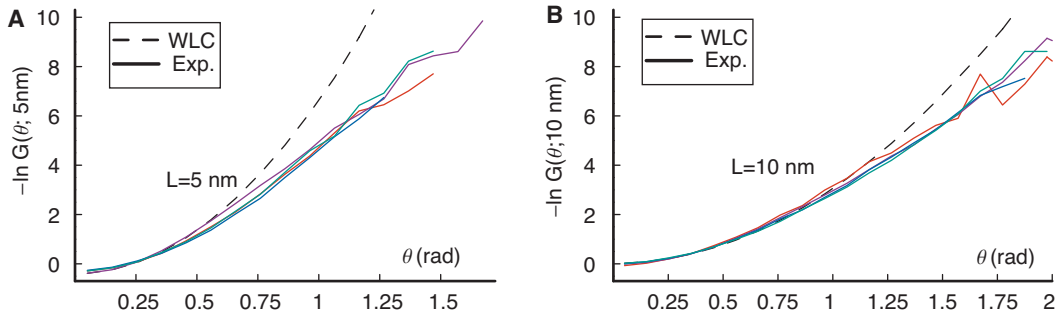

Figure S1: Imaging DNA with a range of salt concentrations does not alter our conclusions. These figures show $G(\theta; L)$ for $[Mg^{2+}] = 6\,\text{mM}$ (*red*), $12\,\text{mM}$ (*purple*), $30\,\text{mM}$ (*blue*), and $150\,\text{mM}$ (*green*). For comparison, the *dashed black curve* is the prediction of WLC (same as dashed lines in Fig. 3**a**). Panel **a:** $L = 5\,\text{nm}$. Panel **b:** $L = 10\,\text{nm}$.

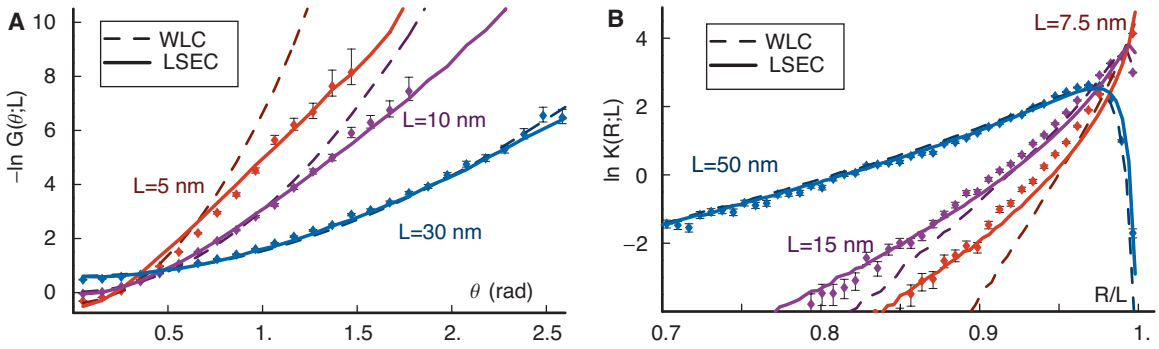

Figure S2: The same graphs as Fig. 3, except that the dots reflect experimental data for DNA incubated with ligase to repair possible nicks.

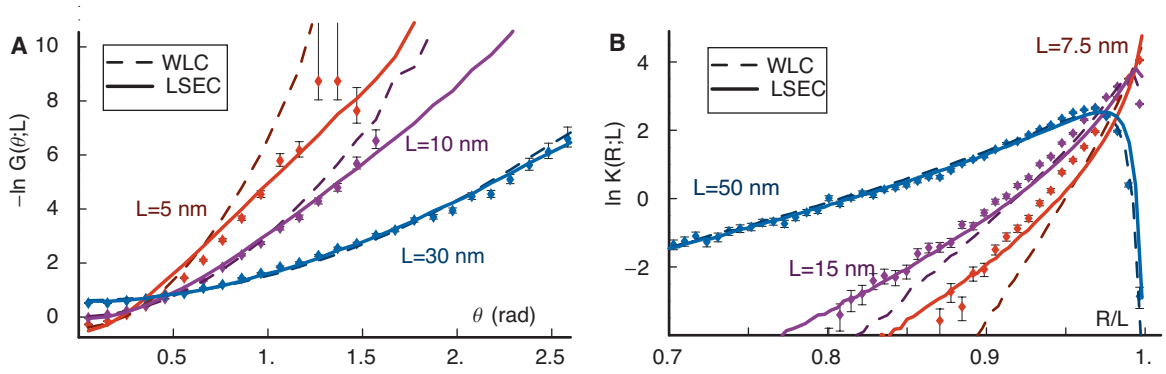

Figure S3: The same graphs as Fig. 3, except that the dots reflect experimental data taken on V1-grade mica.

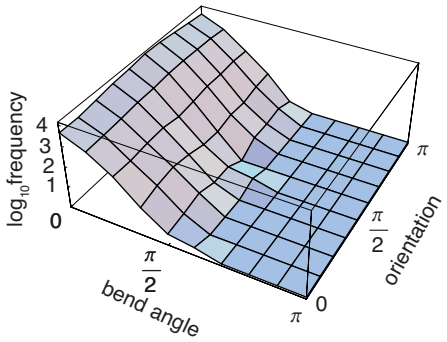

Figure S4: The incidence of large-angle bends is not correlated with any particular direction. The graph is a 2D histogram giving the frequency of bends versus both bend angle and absolute orientation of the tangent relative to the AFM raster. No preference for large-angle bends with any particular orientation is seen.

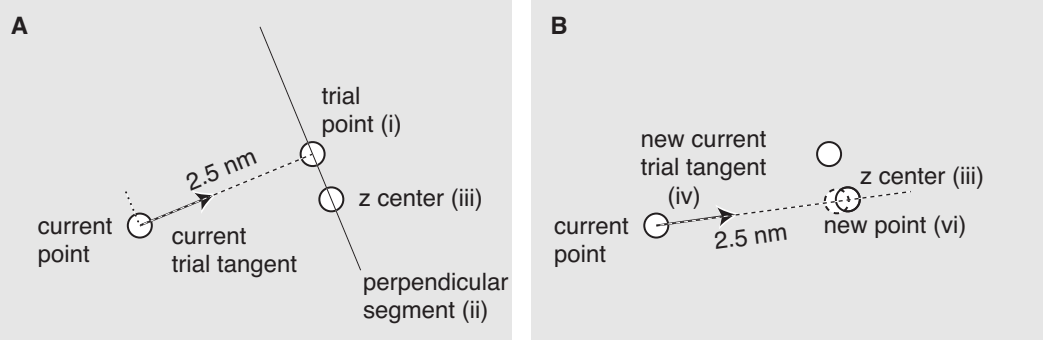

Figure S5: Tracing algorithm. *(i)* A trial point is placed 2.5 nm from the current point in the trial tangent direction. *(ii)* The z height data is interpolated along a segment, centered on the trial point, normal to the trial tangent, and 10 nm in length. *(iii)* The z-weighted center (Eq. (3)) is computed along this segment. *(iv)* A new trial tangent is defined by the ray connecting the current point and the z center. *(v)* Steps i-iv are repeated three times in total. *(vi)* The new current point is defined 2.5 nm along the current trial tangent from the current point.

B.2 Image analysis

The algorithm alluded to in the main text is as follows: *(i)* A trial point is placed 2.5 nm from the current point in the trial tangent direction. *(ii)* The z height data is interpolated along a segment, centered on the trial point, normal to the trial tangent, and 10 nm in length. *(iii)* The z-weighted center

$$\vec{X}_{\mathrm{z\ center}} \equiv \int_0^{10\ \mathrm{nm}} \mathrm{d}s\ Z(\vec{x})\,\vec{x}(s), \tag{3}$$

is computed along this segment, where $Z(\vec{x})$ is the local z height at $\vec{x}$ and $\mathrm{d}s$ is the differential arc length along the segment defined by $\{\vec{x}(s)\}$ (Fig. S5**a**). *(iv)* A new trial tangent is defined by the ray connecting the current point and the z center. *(v)* Steps *i-iv* are repeated three times in total. *(vi)* The next point is then defined by moving $2.5\,\mathrm{nm}$ along the current trial tangent from the current point (Fig. S5**b**). This process is repeated until the end of the chain is reached or the operator manually terminates the trace.

C Monte Carlo evaluation of models

C.1 Monte Carlo code

Our Monte Carlo code was implemented in *Mathematica.* Our code generated sets of discrete 2D chains with random bends chosen from a Boltzmann distribution, with $E(\theta)$ given by E_{WLC} or E_{LSEC}. The required probability distribution functions were then computed and compared to those extracted from the AFM images. Various analytic treatments also permit the evaluation of such distribution functions (*25, 26, 27, 28, 29*).

Each chain began at a random angle relative to the x-axis. We did not enforce an excluded-volume constraint, which is not expected to be a significant effect for the short separations we studied. The parameters (ξ for WLC, and α for our model) were manually adjusted to fit the long-distance distribution G.

C.2 Simulated data

The experimental limitations of atomic force microscopy limit the resolution at which the surface conformation of DNA can be determined. The experimental traces only correspond to the physical conformation above a resolution limit. In this paper, we have analyzed the statistics of DNA at the 5 nm length scale (even though the AFM height measurements were separated by only 1.95 nm), because we can show that, at this resolution, the measured chain statistics reflect the underlying conformation of the chain rather than tracing artifacts.

Several important factors contribute to the resolution limit: pixelation, tip radius, and noise. To investigate the importance of these three factors, we generated extensive simulated AFM data using WLC statistics and then traced using the same algorithm we employed for tracing the real experimental data (Sect. B.2). This procedure allowed us to characterize the effects of pixelation, tip radius, and noise and argue that the measured deviations from the WLC model are not due to limitations in experimental resolution.

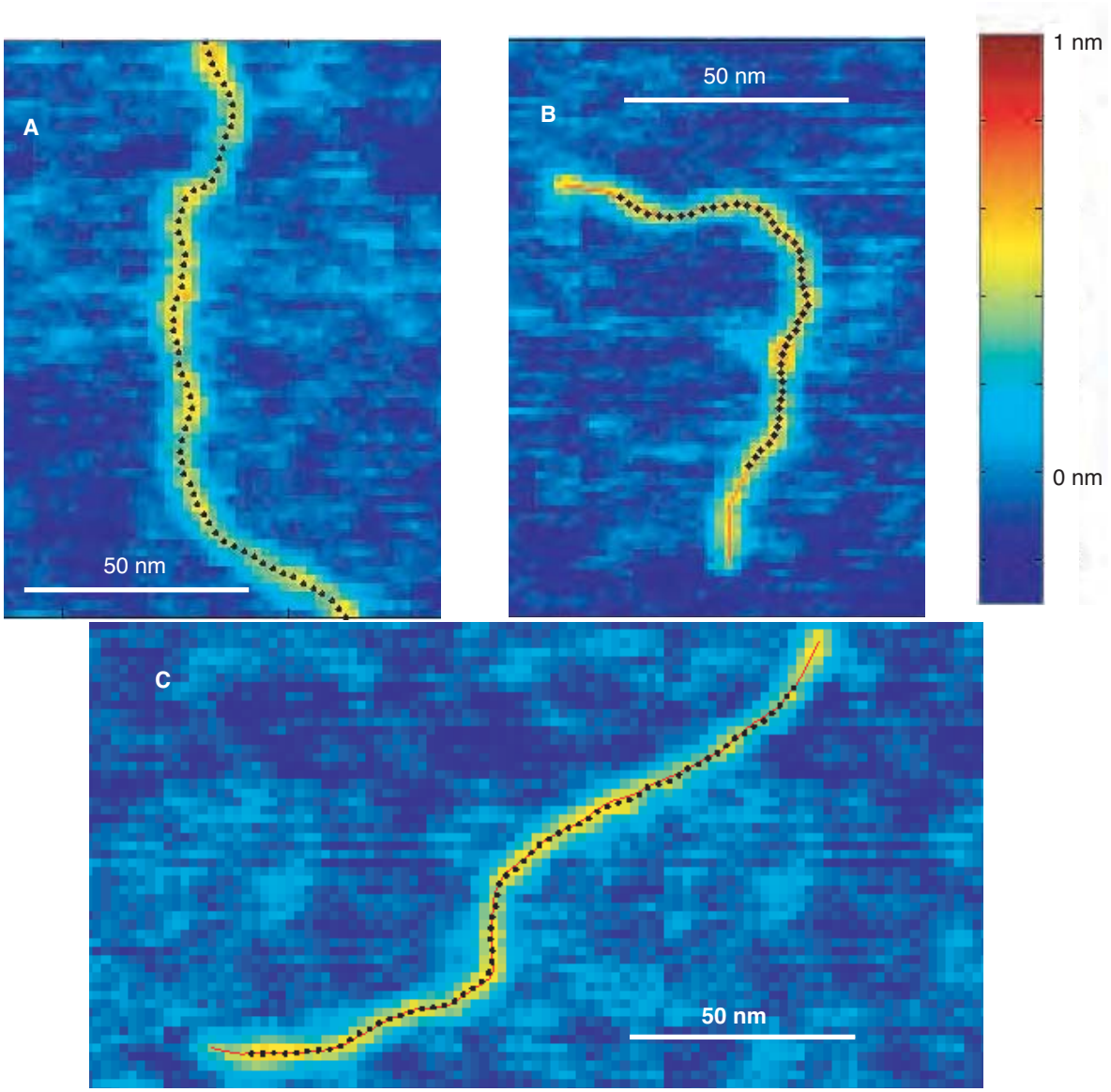

Figure S6: **a.** Example of experimental AFM data *(color)* with inferred DNA contours *(black dots)*. **b.** Example of simulated AFM data, together with the contour found by our tracing algorithm *(black dots)* and the underlying conformation generated by Monte Carlo simulation *(red line)*. In both panels the separation between points is 2.5 nm. **c.** As **(b)**, but with simulated data from our model. Both the underlying chain *(red dots)* and the inferred contour are discretized to the scale $\ell = 2.5$ nm.

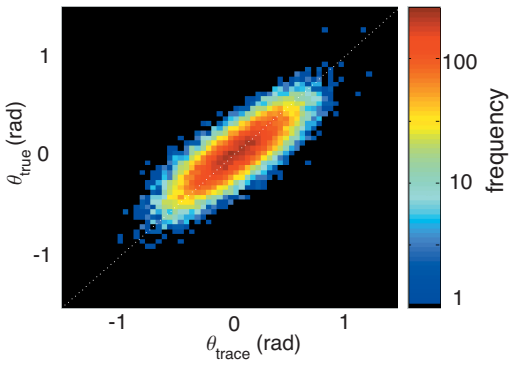

Figure S7: Two dimensional histogram comparing the true bending angle $\theta_{s,s+5\mathrm{nm}}$ of a simulated WLC chain to the corresponding angle reported by our image-processing algorithm. The color scheme denotes the number of counts in angular bins corresponding to pairs $(\theta_{\mathrm{true}}, \theta_{\mathrm{trace}})$. Due to the combined effects of noise and tip convolution, the true deflection angle cannot be determined exactly, resulting in a distribution of traced deflection angles. The dotted diagonal line represents perfect accuracy. Fig. S8 shows that the spread in this distribution does not account for the deviation of our results from the predictions of WLC.

To generate simulated WLC data, we first generate a two-dimensional chain conformation using a Monte Carlo code to implement WLC statistics with persistence length $54\,$nm. The chain discretization length was $0.1\,$nm, much smaller than the pixel size. The effect of the tip convolution was simulated by giving this chain a gaussian height profile with amplitude $0.5\,$nm and full width at half maximum chosen to resemble the observed experimental profiles.

Modeling the noise proved nontrivial because the noise correlation length was found to be longer than a pixel. Therefore, instead of modeling the noise, we assembled a background-noise template from AFM images using regions of mica without DNA. This background noise template had a root-mean-square roughness of $0.06\,$nm. With a randomized x, y spatial offset it was directly added to the z heights generated by the tip convolution simulation. The properties of the noise in the simulated and experimental data were therefore identical in the bulk of the mica. This recipe produced simulated data that were locally indistinguishable from actual AFM data (Fig. S6**a,b**).

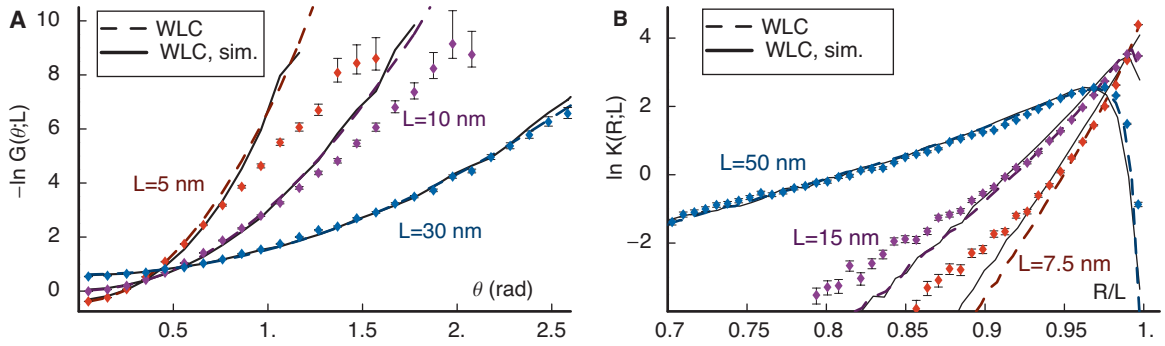

Figure S8: Simulation of instrumental effects does not alter our conclusions. *Dots and colored, dashed lines* are the same as Fig. 3. *Solid curves:* The same distributions when a sample of WLC configurations with $\xi = 54\,\text{nm}$ was generated numerically and converted to simulated AFM data, then subjected to the same image analysis that yielded the experimental dots. The leftmost solid curve in (**a**) is the same as the solid curve in Fig. 2**c**.

The analysis of simulated data provides a series of useful checks and controls. A first important check of the tracing algorithm is simply to overlay the underlying generated conformation and the traced conformation obtained from the corresponding simulated data (Fig. S6**b**). What is most relevant to the discussion in this paper is the error in the traced angles. We have used the simulated data to estimate the distribution in measured angles given an underlying angle (Fig. S6**c**). These calculations show that (on average) tip convolution leads to an underestimate of the underlying deflection angle, whereas noise leads to an overestimate of the deflection angle. These experimental errors cancel to some extent in our experiment: In Fig. S8, the WLC and simulated tangent distribution functions are nearly identical despite broadening caused by noise and narrowing caused by tip convolution (see also Table S2). We found that noise does not significantly distort the histogram of bend frequencies unless its amplitude is taken to be twice what is actually observed in AFM data (data not shown). We are therefore confident that tracing artifacts alone cannot explain the observed short-contour-length deviation from the WLC theory.

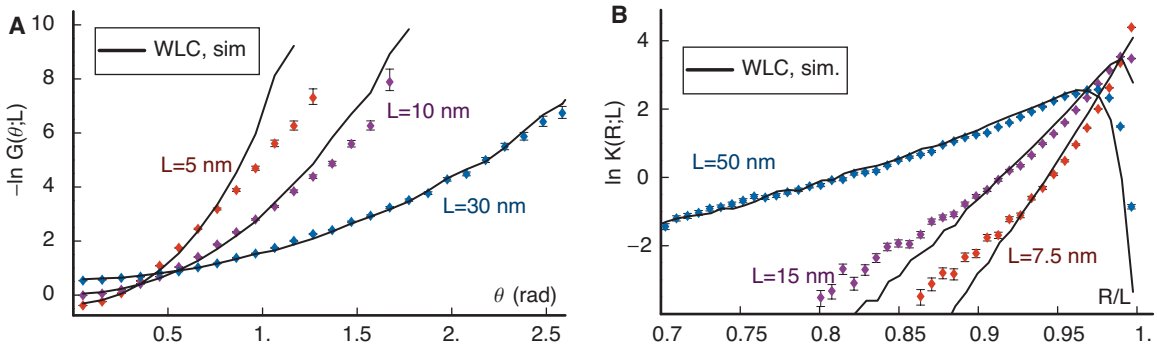

Figure S9: Excising very high-curvature regions does not alter our results. The dots and curves are the same as in Fig. S8, except that here we identified very large bends (angle > 1.5 radian over $L = 7.5$ nm), in both the experimental data and the simulated data, then excluded ± 20 nm regions around each such bend from our analysis. A total of 31 regions were removed from the experimental traces.

C.3 Excise big kinks

It is possible that various effects extrinsic to DNA elasticity could induce large-angle bends, for example, defects on the mica surface. In addition to repeating our results on V1-grade mica (Sect. S3), we checked directly that our conclusions do not rest upon a small set of (possibly anomalous) observations. We did this by excising from the data all points with very large bends, together with a buffer zone about every such point. Then we applied the same procedure to our simulated WLC data and compared (Fig. S9). Apart from the expected truncation of our curves at the high-angle end, we saw no significant change after this procedure; the data still exclude WLC.

D Other calculations

D.1 Force–extension and Cyclization

To demonstrate the experimental implications of the measured DNA tangent distribution function, we have computed both the force extension of the polymer as well as the cyclization J factor (Fig. S10). The computational tools employed in these calculation are described elsewhere (*7*). (Analogous calcu-

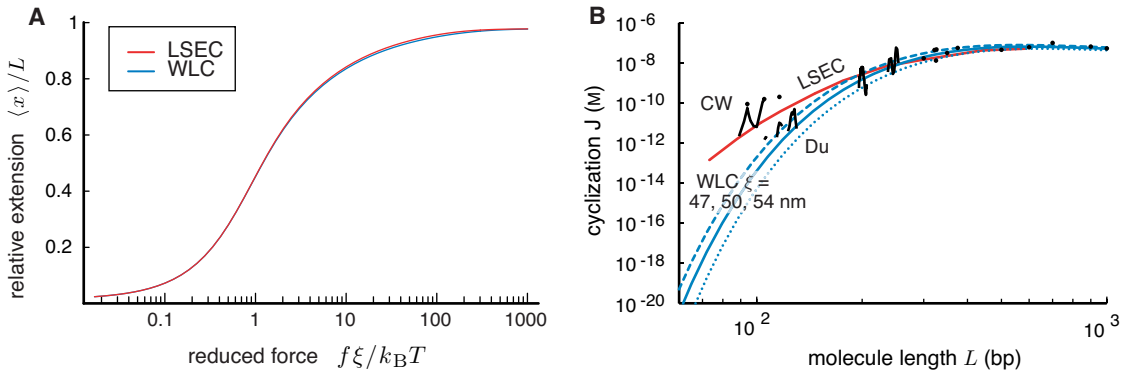

Figure S10: Our model agrees with WLC for other experimentally observable quantities. **a**. Semilog plot comparing the force versus extension relations for the 3D WLC and our model, calculated with the same 3D persistence length $\xi = 50\,\mathrm{nm}$ (*7*). Despite the dissimilar short-length-scale tangent distribution function, the entropic stretching behavior of the two models is nearly identical. (For forces greater than $\approx 20\,\mathrm{pN}$, intrinsic stretch becomes important, and neither model is expected to be accurate.) **b**. The cyclization J factor probes high-curvature chain statistics. This log-log plot shows the cyclization J factor (in units of molarity) for WLC (*blue curves*) and our model (*red curve*) models and compares with experimental measurements (*dots*); see experimental papers cited in (*7*). The theoretical curves do not include the periodic modulation visible in the continuous sets of experimental data (*solid black curves*), because we neglect twist stiffness in this paper. Our arguments predict that our model will be identical to WLC for long DNA constructs, as shown. But, for DNA shorter than $\approx 200\,\mathrm{bp}$, the short-contour-length chain statistics become important and our model's J factor diverges from the WLC prediction. In fact, for $94\,\mathrm{bp}$ sequences, our J factor is three orders of magnitude larger than that predicted by the WLC model. Measurements by Cloutier and Widom (*16, 4*) (*black curves labeled CW*) and by Du et al. (*17*) (*black curves labeled Du*) are shown for comparison.

lations in kinkable WLC models were given in Refs. (*12, 13, 14, 30, 15*).)

D.2 Nematic ordering

We found that the experimental data coming from the same sample had a bias toward tangent vectors pointing along a particular direction in the sample (visible in the low-angle region of Fig. S4). This direction was not aligned with, nor perpendicular to, the AFM raster scan lines. Presumably this bias

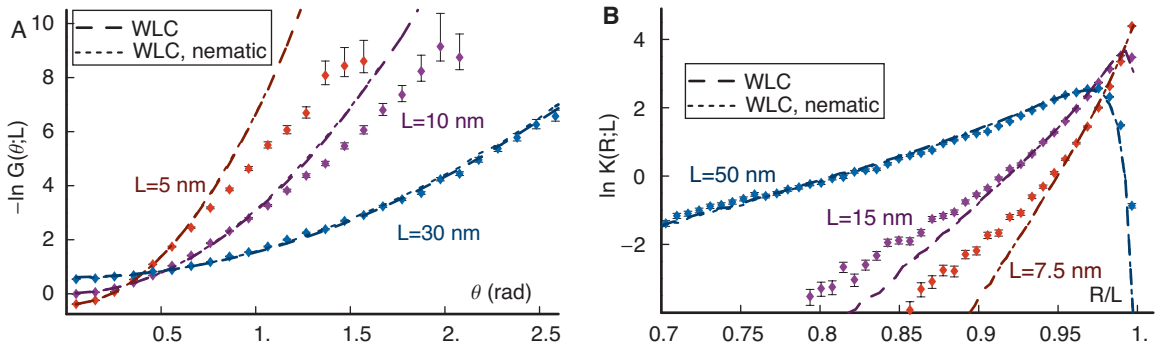

Figure S11: The small anisotropy visible in the distribution of absolute angles does not affect the distributions studied here. **a,b.** *Points, dashed lines:* The same as the points and dashed lines in Fig. 3. *Dotted lines:* Probability distributions calculated using the same WLC energy function as was used in the dashed lines, with an additional ordering term. The value of the angular bias parameter λ was chosen to duplicate the slight preference for one overall orientation seen in Fig. S4.

was created by hydrodynamic effects during the washing step. Although we expected that the statistical measures we used would be largely unaffected by this bias, we nevertheless modeled it roughly by adding an ordering term $-\frac{\lambda\ell}{2}\cos(2\psi)k_{\mathrm{B}}T$ to the energy function, where ψ is the angle relative to the preferred direction and λ is a constant. We implemented the effect of this term by weighting each generated chain by $\exp((\lambda/2)\sum_i \ell\cos(2\psi_i))$. Choosing $\lambda = 0.013\,\mathrm{nm}^{-1}$ reproduced the observed histogram of absolute angles, but had no discernible effect on the distributions G or K, as expected (Fig. S11). In particular, this effect cannot explain the discrepancy between the experimental data and those predicted by WLC. As a check on the Monte Carlo code, we also found an analytical formula for $G(\theta; L)$ in WLC in the presence of the aligning field, by an extension of the methods in Refs. (*26*, *28*); again we found that the angle bias had little effect.

D.3 Not kinkable WLC

Fig. S12 compares our data with a version of the "kinkable WLC" model proposed in Refs. (*13*)–(*12*). To obtain the curve, we used the formula (*13*)

$$E_{\mathrm{KWLC}}(\theta)/k_{\mathrm{B}}T = -C\ln\left[\mathrm{e}^{-\xi_0\theta^2/(2\ell_1)} + \frac{1}{2}\zeta(\ell_1)^2/\xi_0\right] \tag{4}$$

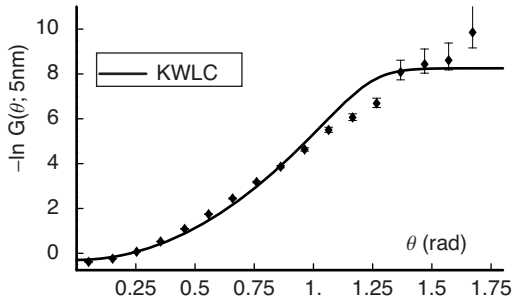

Figure S12: Our data are not better described by the "kinkable WLC" model. The *dots* are the same as in Fig. 2**c**. The highest point shown corresponded to an angular bin containing just one count. It was therefore omitted from other graphs in this paper, but serves here to give a lower bound on G at very large angles. *Solid curve:* The analytic formula, Eq. (4), divided by $k_{\rm B}T$.

Here ξ_0 is a "bare" bending stiffness, related to the full $\xi = 54\,$nm by $\xi = \frac{\xi_0}{1+\zeta\xi_0}$, $\ell_1 = 5\,$nm, and C is a normalization constant. Taking $\zeta\xi_0 = 0.05$ leads to enhanced cyclization as seen in some experiments (*13*), and also leads to a probability distribution of bends corresponding to the curve in Fig. S12. Our experimental data do not follow the prediction made by this model; our bend distribution deviates from a harmonic form for $\theta > 0.6\,$radian, then continues to decline (so $-\ln\ G(\theta; 5\,\text{nm})$ rises) instead of leveling off.

Note that if surface adsorption either induced nicks in the DNA, or allowed preexisting nicks to become free hinges, then we would expect a KWLC form for the histogram, contrary to the above observation.

D.4 Rounded energy function

In addition to the two choices $E_{\rm WLC}$ and $E_{\rm LSEC}$, we also studied a family of energy functions $E(\theta)$ discretized at $\ell = 2.5\,$nm and interpolating between these extremes. These functions were quadratic for values of θ less than some θ_0 and thereafter followed a linear rule like Eq. (1). In each case adjusting the slope α to fit the long-scale distributions, we found that the best match was obtained with our model

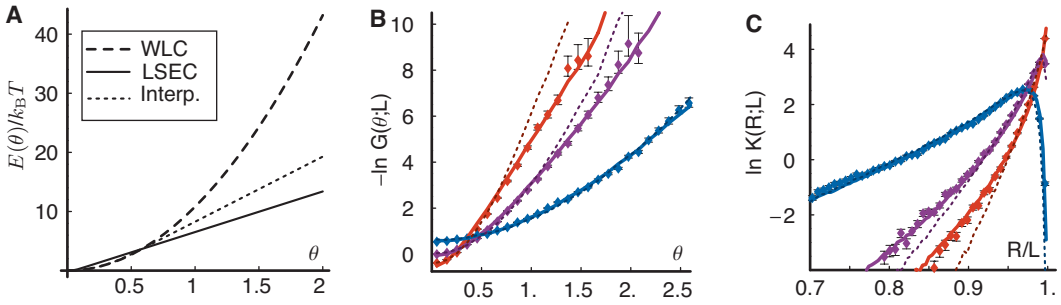

Figure S13: Our model (Eq. (1)) fits our data better than any of a family of local elasticity models interpolating between it and WLC. **a.** *Dotted line:* Trial $E_{\mathrm{interp}}(\theta)$ interpolating between WLC and our model. *Dashed line:* $E_{\mathrm{WLC}}(\theta)$, the function used in the Monte Carlo calculation leading to the dashed lines in Fig. 3. *Solid line:* $E_{\mathrm{LSEC}}(\theta)$, the function used to make the solid lines in Fig. 3. In each case, the curvature of the energy function was selected to reproduce the observed distributions $G(\theta; L)$ and $K(R; L)$ of the experimental data at long separations L. **b,c.** *Solid lines:* The same as solid lines in Fig. 3. *Dotted lines:* The corresponding probability distributions calculated using $E_{\mathrm{interp}}(\theta)$.

(the case $\theta_0 = 0$) (Fig. S13). As mentioned earlier, however, with other choices for the discretization scale even our model gives a rounded distribution (see Fig. 3**a**).

D.5 Comparison to Du et al.

As mentioned earlier, Du et al. obtained a bending-energy function by analysis of known DNA trajectories in protein–DNA complexes (*17*). Although, as they noted, this procedure yielded an energy function with a much shorter persistence length than that of free DNA, nevertheless it is noteworthy that their function also corresponds to nonlinear DNA elasticity, and that when coarsegrained to the scale of 5 nm it has the same roughly linear form as the one we found.

Fig. S14 shows the phenomenological bending energy function found by Du et al., and its form when coarsegrained to the scale 2.5 nm. The graphs show that even at 2.5 nm, this bending energy function differs greatly from the corresponding WLC form, and qualitatively shows the same linear behavior at large angles as our model (Eq. (1)). As remarked by Du et al., their bending energy function

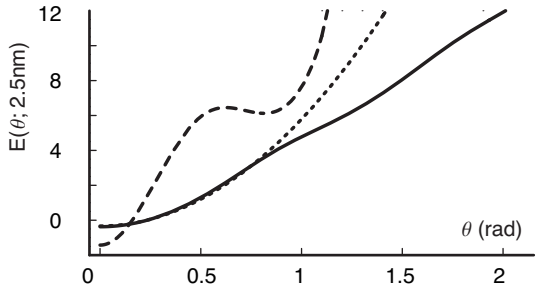

Figure S14: Phenomenological bending energy function found by Du et al. from analysis of protein-DNA complexes. *Dashed curve:* Minus the natural logarithm of the incidence of bends of various angles between successive basepairs, from Ref. (*17*). *Solid curve:* Corresponding 2D bending energy function coarse-grained to the scale 2.5 nm, obtained by convolving the dashed curve with itself 7.35 times. The *dotted curve* shows a WLC bending energy function at this same scale and with the same persistence length as the solid curve (about 31 nm).

should not be interpreted as a quantitative measurement, because it is based on DNA conformations under external stress. However, its general form does point to an elastic breakdown similar to the one we measure in this paper.

E Out-of-equilibrium adsorption model

The experimental method of imaging the DNA molecule involves trapping the chain on a mica surface. In the main text, we assumed that the bound DNA strand undergoes thermal conformational fluctuations and achieves chain statistics that represent equilibrium behavior in two dimensions. However, it is conceivable that the process of adsorption incurs kinks in the conformation that are long-lived and influence the chain statistics; in this case, our results could not be used to draw conclusions about the elasticity of DNA in solution. To rule out this possibility, we explored the nonequilibrium process of polymer adsorption and subsequent relaxation using Brownian dynamics simulation (*31, 32*). We find that the experimental behavior cannot be attributed to such nonequilibrium adsorption.

Polymer adsorption can dramatically affect the chain geometry and statistics, as demonstrated in

a number of works (*33, 34, 35, 36, 37, 38, 39*). However, the effect of nonequilibrium adsorption of semiflexible polymers is still not well understood. We modeled the polymer strand as a discrete chain of beads with a quadratic potential for bending and stretching (*31, 32*). We neglected self-avoidance for our short polymer length, assuming that the instances of chain crossing during adsorption are negligible and that chain crossing after adsorption is attributed to chain segments passing over-and-under each other. The bending modulus was chosen to give a free persistence length of 53 nm, and the stretching modulus was sufficiently large to make the chain effectively inextensible. The chain dynamics are governed by a Langevin equation with a local drag force that is linear in the segment velocity, thus we neglected polymer-polymer and polymer-surface hydrodynamic interactions. For this simple test, we assumed the polymer mobility in solution is much larger than the mobility of the surface-bound polymer.

We ran two simulations to explore the adsorption behavior. In the first simulation, we took a pre-equilibrated polymer chain (by Monte Carlo simulation) and allowed it to freely fluctuate next to an adsorbing surface. Any chain segment that touches the surface is frozen; we ran the simulation until all of the chain segments were fixed on the surface. In the second simulation, we took the adsorbed conformation from the first simulation and performed a simulation of its dynamics while confined on the adsorbing surface. This two-step simulation process implicitly assumes that the adsorption is effectively instantaneous in comparison to the subsequent surface relaxation, *i.e.* the surface mobility is much smaller than the free-chain mobility.

Fig. S15**c** shows a typical snapshot of the surface-bound polymer just after the nonequilibrium adsorption process (defined as time zero). This conformation exhibits several tightly bent chain segments, particularly at the left-most end of the chain. These bent segments influence the chain statistics by enhancing the probability of large bending angles. This is manifest in the tangent-tangent correlation function $G(\theta; L, t)$ shown in Fig. S15**a**, where we define this quantity as the distribution function averaged over the chain length as well as over an ensemble of simulations after a given time t of surface relaxation after the adsorption process is complete. We measure time in terms of the Brownian time scale $\tau_B = \eta\ell^2/(k_{\rm B}T)$ where η is the DNA drag coefficient on the surface (unknown value), ℓ is the

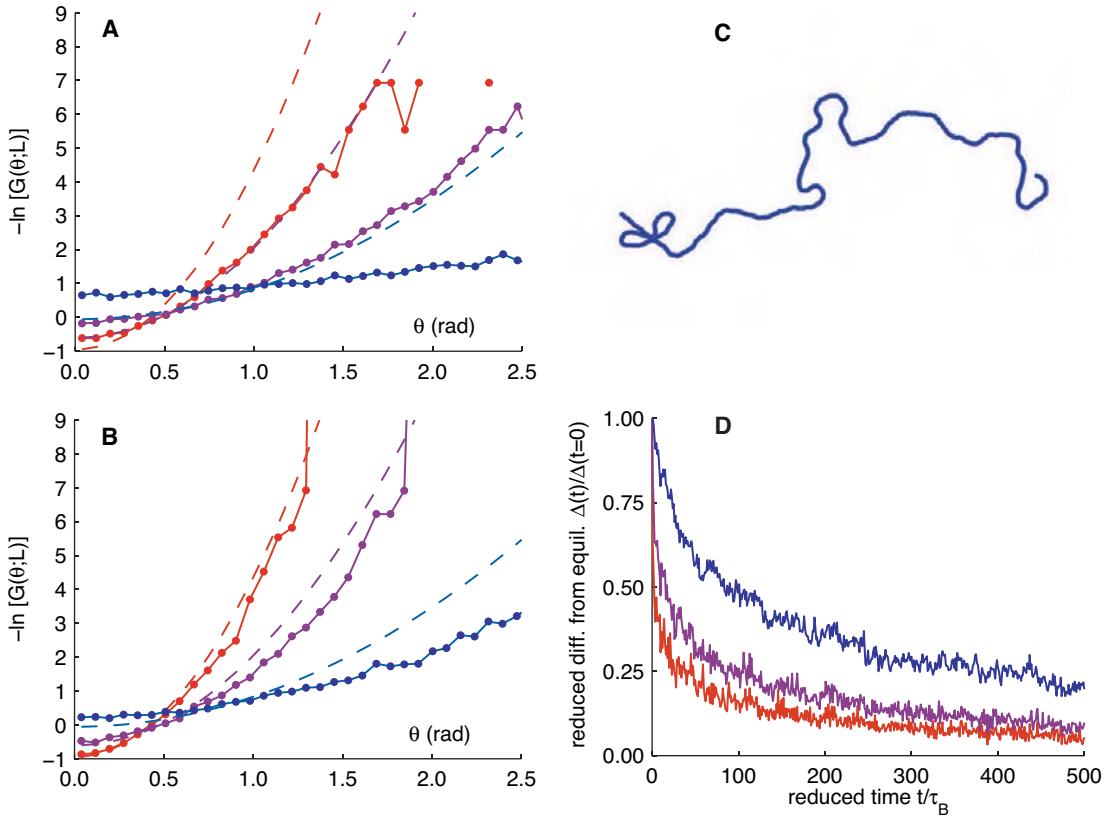

Figure S15: The influence of nonequilibrium adsorption on the chain statistics. **a.** Tangent-tangent correlation function $G(\theta; L, t)$ just after adsorption ($t = 0$), for separation lengths L of 5 nm (*red*), 10 nm (*purple*), and 30 nm (*blue*). Our simulation results (*solid curves*) and their corresponding equilibrium behavior of the wormlike chain model in two dimension (*dashed curves*) are provided in each plot. **b.** The same after time $t = 500\tau_B$ of subsequent surface relaxation. **c.** Typical snapshot of a semiflexible polymer irreversibly adsorbed on a planar surface determined by Brownian dynamics simulation. **d.** Average variance between the tangent-tangent correlation function from our simulations and from the wormlike chain model versus time t/τ_B.

interbead spacing (2.5 nm), and $k_{\mathrm{B}}T$ is the thermal energy (4.1 pN nm). Fig. S15**a** shows the tangent-tangent distribution function just after adsorption ($t = 0$), for various separation lengths L; panel **b** shows the same after time $t = 500\tau_B$ of subsequent surface relaxation. We include in Fig. S15 the

simulation results (solid curves) and their corresponding curves for the equilibrium behavior of the wormlike chain model in two dimensions (dashed curves).

The tangent-tangent correlation functions from our simulations exhibit a similar trend as our experiments: Large deformation angles are enhanced relative to the wormlike chain model. However, the deviation from the equilibrium wormlike chain curves for our simulation data becomes larger for larger lengths, in contrast with the experimental data which tend to the wormlike chain curves at larger distance separation. Thus, we conclude from the simulation results shown in Fig. S15 that the experimental data cannot be not explained by nonequilibrium adsorption of a wormlike chain on the surface.

There is the possibility, however, that subsequent relaxation of the chain after adsorption could cause the chain statistics to approach the wormlike chain model in such a manner that they approach our experimental data. However, the results shown in Fig. S15**b** demonstrate the expected length dependence of relaxation: short length scales relax faster than long length scales (*40, 41, 42*). To show this more clearly, we define the variance from the wormlike chain model as

$$\Delta = \int_0^\pi d\theta \left[G(\theta; L, t) - G_{\mathrm{WLC}}(\theta; L)\right]^2, \tag{5}$$

where $G_{\mathrm{WLC}}(\theta; L)$ is the equilibrium tangent-tangent correlation function for the 2D wormlike chain model. We plot in Fig. S15**d** the variance Δ versus time for various length separations L. Fig. S15 shows that upon subsequent relaxation after nonequilibrium adsorption the statistics for short chain length separation reach equilibrium faster than long chain length separation. In other words, nonequilibrium adsorption does not explain our experimental data, and subsequent relaxation takes the statistical behavior further from the experimental results.

These simulations focus on only one scenario where out-of-equilibrium physics impacts the chain statistics. However, the conclusions that are drawn from these simulations typify the nonequilibrium effect. Namely, the statistical behavior at long length scales relaxes slower than the behavior for short length separation (*40, 41, 42*), as demonstrated in our simulations. The experiments show that the short length behavior deviates from the expected equilibrium, but the experimental distribution displays the expected equilibrium behavior at longer length scales. This effect is inconsistent with the trends demon-

strated in our simulations. Therefore, we conclude that the nonequilibrium nature of DNA adsorption does not explain our experimental results.

References

1. Yamakawa, H. *Helical Wormlike Chains in Polymer Solutions* (Springer, Berlin, 1997).

2. Popov, Y. O. & Tkachenko, A. V. Effects of sequence disorder on DNA looping and cyclization (2005). Unpublished (`http://arxiv.org/abs/cond-mat/0510302`).

3. Swigon, D., Coleman, B. D. & Olson, W. K. Modeling the Lac repressor–operator assembly: The influence of DNA looping on lac repressor conformation. *Proc. Natl. Acad. Sci. USA* Published online June 19, 2006, 10.1073/pnas.0603557103.

4. Cloutier, T. E. & Widom, J. DNA twisting flexibility and the formation of sharply looped protein–DNA complexes. *Proc. Natl. Acad. Sci. USA* **102**, 3634–3650 (2005).

5. Nelson, P. *Biological Physics: Energy, Information, Life* (W. H. Freeman and Co., New York, 2004).

6. Schurr, J. M., Delrow, J. J., Fujimoto, B. S. & Benight, A. S. The question of long-range allosteric transitions in dna. *Biopolymers* **44**, 283–308 (1997).

7. Additional mathematical details for the SEC class of models appear in P. A. Wiggins and P. C. Nelson. Generalized theory of semiflexible polymers. *Phys. Rev.* **E73**, 031906 (2006).

8. Rivetti, C., Guthold, M. & Bustamante, C. Scanning force microscopy of DNA deposited onto mica: Equilibration versus kinetic trapping studied by statistical polymer chain analysis. *J. Mol. Biol.* **264**, 919–932 (1996).

9. Hogan, M. E., Rooney, T. F. & Austin, R. H. Evidence for kinks in DNA folding in the nucleosome. *Nature* **328**, 554–557 (1987).

10. Richmond, T. J. & Davey, C. A. The structure of DNA in the nucleosome core. *Nature* **423**, 145–150 (2003).

11. van Noort, J. *et al.* The coiled-coil of the human rad50 DNA repair protein contains specific segments of increased flexibility. *Proc. Natl. Acad. Sci. USA* **100**, 7581–7586 (2003).

12. Yan, J. & Marko, J. F. Localized single-stranded bubble mechanism for cyclization of short double helix DNA. *Phys. Rev. Lett.* **93**, 108108 (2004).

13. Wiggins, P. A., Nelson, P. C. & Phillips, R. Exact theory of kinkable elastic polymers. *Phys. Rev. E* **71**, 021909 (2005).

14. Ranjith, P., Kumar, P. B. S. & Menon, G. I. Distribution functions, loop formation probabilities, and force-extension relations in a model for short double-stranded DNA molecules. *Phys. Rev. Lett.* **94**, 138102 (2005).

15. Yan, J., Kawamura, R. & Marko, J. F. Statistics of loop formation along double helix DNAs. *Phys. Rev. E* **71**, 061905 (2005).

16. Cloutier, T. E. & Widom, J. Spontaneous sharp bending of double-stranded DNA. *Molecular Cell* **14**, 355–362 (2004).

17. Du, Q., Smith, C., Shiffeldrim, N., Vologodskaia, M. & Vologodskii, A. Cyclization of short DNA fragments and bending fluctuations of the double helix. *Proc Natl Acad Sci USA* **102**, 5397–402 (2005).

18. Shroff, H. *et al.* Biocompatible force sensor with optical readout and dimensions of 6 nm^3. *Nano Lett.* **5**, 1509–1514 (2005).

19. Hochschild, A. & Ptashne, M. Cooperative binding of lambda-repressors to sites separated by integral turns of the DNA helix. *Cell* **44**, 681–687 (1986).

20. Song, L. & Schurr, J. Dynamic bending rigidity of DNA. *Biopolymers* **30**, 229–237 (1990).

21. Rivetti, C., Walker, C. & Bustamante, C. Polymer chain statistics and conformational analysis of dna molecules with bends or sections of different flexibility. *J. Mol. Biol.* **280**, 41–59 (1998).

22. Nelson, P. Sequence-disorder effects on DNA entropic elasticity. *Phys. Rev. Lett.* **80**, 5810–5812 (1998).

23. Vologodskaia, M. & Vologodskii, A. Contribution of the intrinsic curvature to measured DNA persistence length. *J. Mol. Biol.* **317**, 205–213 (2002).

24. Podesta, A. *et al.* Positively charged surfaces increase the flexibility of DNA. *Biophysical Journal* **89**, 2558–2563 (2005).

25. Stepanow, S. & Schutz, G. M. The distribution function of a semiflexible polymer and random walks with constraints. *Europhys. Lett.* **60**, 546 (2002).

26. Spakowitz, A. J. & Wang, Z.-G. Exact results for a semiflexible polymer chain in an aligning field. *Macromolecules* **37**, 5814–5823 (2004).

27. Hamprecht, B., Janke, W. & Kleinert, H. End-to-end distribution function of two-dimensional stiff polymers for all persistence lengths. *Phys. Lett. A* **330**, 254 (2004).

28. Spakowitz, A. J. & Wang, Z.-G. End-to-end distance vector distribution with fixed end orientations for the wormlike chain model. *Phys. Rev. E* **72**, 041802 (2005).

29. Spakowitz, A. J. Wormlike chain statistics with twist and fixed ends. *Europhys. Lett.* **73**, 684–690 (2006).

30. Popov, Y. O. & Tkachenko, A. V. Effects of kinks on DNA elasticity. *Phys. Rev. E* **71**, 051905 (2005).

31. Allison, S., Austin, R. & Hogan, M. Bending and twisting dynamics of short linear DNAs - analysis of the triplet anisotropy decay of a 209-basepair fragment by Brownian simulation. *J. Chem. Phys.* **90**, 3843–3854 (1989).

32. Chirico, G. & Langowski, J. Kinetics of DNA supercoiling studied by Brownian dynamics simulation. *Biopolymers* **34**, 415–433 (1994).

33. Cerda, J. J. & Sintes, T. Stiff polymer adsorption. Onset to pattern recognition. *Biophysical Chemistry* **115**, 277–283 (2005).

34. Chakraborty, A. K. & Golumbfskie, A. J. Polymer adsorption — Driven self-assembly of nanostructures. *Ann. Rev. Phys. Chem.* **52**, 537–573 (2001).

35. Kuznetsov, D. V. & Sung, W. Semiflexible polymers near attracting surfaces. *Macromolecules* **31**, 2679–2682 (1998).

36. Netz, R. R. & Joanny, J. F. Adsorption of semiflexible polyelectrolytes on charged planar surfaces: Charge compensation, charge reversal, and multilayer formation. *Macromolecules* **32**, 9013–9025 (1999).

37. Semenov, A. N. Adsorption of a semiflexible wormlike chain. *Euro. Phys. J. E* **9**, 353–363 (2002).

38. Stepanow, S. Adsorption of a semiflexible polymer onto interfaces and surfaces. *J. Chem. Phys.* **115**, 1565–1568 (2001).

39. Van der Linden, C. C., Leermakers, F. A. M. & Fleer, G. J. Adsorption of semiflexible polymers. *Macromolecules* **29**, 1172–1178 (1996).

40. Doi, M. & Edwards, S. F. *The Theory of Polymer Dynamics* (Oxford University Press Inc., New York, NY, 1986).

41. MacKintosh, F. C., Käs, J. & Janmey, P. A. Elasticity of semiflexible biopolymer networks. *Phys. Rev. Lett.* **75**, 4425 (1995).

42. Pasquali, M., Shankar, V. & Morse, D. C. Viscoelasticity of dilute solutions of semiflexible polymers. *Phys. Rev. E* **6402**, 020802 (2001).